Tailoring the magnetic anisotropy, magnetization reversal, and anisotropic magnetoresistance of Ni films by ion sputtering

Hao-liang Liu,[1] Tomáš Škereň,[2] Alexander Volodin,[1] Kristiaan Temst,[2] André Vantomme,[2] and Chris Van Haesendonck[1,*]
[1] *KU Leuven, Laboratorium voor Vaste-Stoffysica en Magnetisme, Celestijnenlaan 200 D, BE-3001 Leuven, Belgium*
[2] *KU Leuven, Instituut voor Kern- en Stralingsfysica, Celestijnenlaan 200 D, BE-3001 Leuven, Belgium*
(Received 15 November 2014; revised manuscript received 12 February 2015; published 5 March 2015)

We studied surface morphology induced changes of magnetic anisotropy, magnetization reversal, and symmetry of the anisotropic magnetoresistance (AMR) in ion sputtered Ni films grown on MgO (001). Grazing-incidence ion sputtering generally develops anisotropic surface roughness of the Ni films, i.e., nanometer wide ripples parallel to the ion beam direction, giving rise to uniaxial magnetic anisotropy with the easy axis along the ion beam direction. The formed ripples act as domain wall nucleation and pinning sites during magnetization reversal, while two-jump domain wall motion dominates in the as-grown Ni films. More importantly, the azimuthal angular dependence of the AMR indicates a superposition of twofold symmetry and fourfold symmetry. By relying on grazing-incidence ion sputtering along specific crystallographic directions, we are able to tailor the relative weight of twofold and fourfold symmetry of AMR. We demonstrate that in contrast to the bulk case, the symmetry of the AMR becomes also sensitive to the surface morphology in thin films, which is in particular relevant for the design of magnetotransport based sensors.

DOI: 10.1103/PhysRevB.91.104403 PACS number(s): 75.60.Jk, 75.30.Gw

I. INTRODUCTION

The artificial engineering of magnetic properties of metallic or semiconductor thin-film magnets by modulating the surface/interface morphology has attracted significant attention for its great importance in both fundamental research and potential applications [1–4]. In particular, grazing-incidence ion beam sputtering has been demonstrated as a reliable tool to manipulate the magnetic anisotropy. The sputtering results in the development of nanoscale surface ripples, giving rise to an in-plane uniaxial magnetic anisotropy (UMA) with controllable orientation and strength through the sputtering conditions [5–9]. Bisio *et al.* employed ion beam sputtering to achieve step-induced UMA in Fe films on flat Ag (001) substrates [10]. Liedke *et al.* engineered the UMA of ferromagnetic thin films without affecting the intrinsic cubic anisotropy by creating nanoscale ripples on various substrates prior to the film deposition [11,12].

Anisotropic magnetoresistance (AMR) has been widely used for studying magnetic anisotropy and magnetization reversal in ferromagnetic thin films, especially for its insensitivity to semiconducting or insulating substrates [13–15]. The AMR originates from spin-orbit coupling, which induces mixing of the spin-up and spin-down density of states of the d electrons. The mixing depends on the magnetization direction, leading to a magnetization direction dependent s-d scattering rate in ferromagnetic metals. In polycrystalline materials the AMR is solely dependent on the angle φ between the current $\mathbf{I}$ and magnetization $\mathbf{M}$: $R = R_\perp + (R_\parallel - R_\perp)\cos^2\varphi$, where $R_\perp$ and $R_\parallel$ are the resistance when $\mathbf{I}\parallel\mathbf{M}$ and $\mathbf{I}\perp\mathbf{M}$, respectively. For polycrystalline materials, the angular dependence of the AMR in general shows twofold symmetry and the magnetocrystalline anisotropy effect is averaged out due to the presence of the randomly oriented grains. In contrast, other symmetries for the angular dependence of the AMR, which reflect the various magnetocrystalline anisotropies, may appear in single-crystalline materials [16]. Fourfold symmetry of the AMR, which corresponds to the appearance of an extra higher-order term proportional to $\cos^4\varphi$ in the AMR, has been observed first in bulk Fe and Ni single crystals and has been reported afterwards for various epitaxial thin films. However, the AMR in the films is considerably reduced due to surface scattering [15,17,18]. The origin of the higher-order term in the AMR in thin films has been related mainly to the crystal symmetry, magnetocrystalline anisotropy, and antiphase boundaries [15,19–21].

Here, we investigate the tailoring of magnetic anisotropy and magnetization reversal by relying on measurements of the AMR of ion sputtered Ni films grown on MgO (001) substrates. The rippling of the surface of the Ni films, which results from grazing-incidence ion sputtering, is able to induce UMA that can be mainly attributed to the presence of a dipolar stray field. The magnetization reversal proceeds by two-jump domain wall motion in the as-grown Ni films and is replaced by domain wall nucleation and pinning along the ripples in the ion sputtered films, resulting in coherent rotation of the magnetization when the applied magnetic field is oriented along a hard crystal axis. Remarkably, the azimuthal angular dependence of the AMR, which reveals a superposition of twofold and fourfold symmetry in the epitaxially grown Ni films, is also directly affected by the surface morphology. We thus demonstrate that nanoscale modifications of the surface morphology in epitaxial films directly affects the AMR, which is crucial for designing novel magnetotransport based devices.

II. EXPERIMENTAL

Crystalline Ni (001) films were deposited on MgO (001) substrates by molecular beam epitaxy at a base pressure of 2×10^{-10} mbar [22]. The substrate was annealed at 600 °C for one hour to remove adsorbed gases on the surface prior to deposition. A series of samples were grown with nominal thickness of 23 nm (sample 1) and 50 nm (samples 2, 3, and 4)

*chris.vanhaesendonck@fys.kuleuven.be

 ©2015 American Physical Society

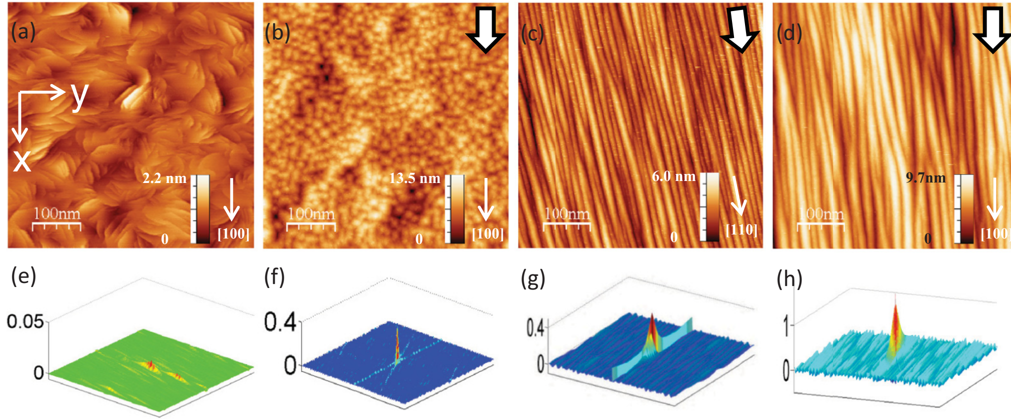

FIG. 1. (Color online) (a)–(d) Large scale STM topography images of samples 1, 2, 3, and 4. (e)–(h) The corresponding two-dimensional correlation function $g(x,y)$ calculated from the height profiles obtained from the STM topography images.The arrows in (b)–(d) indicate the incident ion beam directions projected on the film plane.

while keeping the temperature of the substrate at 180 °C. The surface morphology was characterized by *in situ* scanning tunneling microscopy (STM). Figure 1(a) presents an STM topography image of sample 1. The surface morphology contains atomically flat terraces separated by steps or dislocations, and the average root-mean-square (rms) roughness is about 0.2 nm. Subsequently, sample 2 was irradiated by a 2 keV Ar^+ ion beam at an angle of incidence of 45° with respect to the film normal and along the [100] direction of the substrate with a fluence of 485 ± 25 ions/nm^2. This results in the formation of mound structures on the surface with rms roughness of 1.7 nm [see Fig. 1(b)] [22]. The average mound spacing is about 20 nm. Samples 3 and 4 were irradiated by a 5 keV Ar^+ ion beam at an angle of incidence of 80° with respect to the film normal and along the [110] and [100] directions of the substrates with a fluence of 370 ± 20 ions/nm^2, which leads to the formation of ripple structures with rms roughness of 0.9 and 1.4 nm [see Figs. 1(c) and 1(d)]. The wavelengths of the ripple structures in sample 3 and in sample 4 are 14 nm and 18 nm, respectively. The residual film thicknesses of samples 2, 3, and 4 as measured by x-ray reflectivity are 23.5, 28.7, and 22.7 nm, respectively. For the data analysis we neglect the influence of strain in the different samples since the strain is almost fully relaxed during growth, as can be concluded from both the large number of screw dislocations in the high-resolution STM topography images (not shown) and the results of x-ray diffraction measurements.

In order to further characterize the magnetic properties of the samples, AMR measurements were performed both at room temperature (RT) and at 10 K (LT) in a helium flow cryostat equipped with a three-dimensional vector magnet. This allows measuring the angular dependence of the AMR without rotating the sample [23]. The AMR is measured in approximately 1.5 mm × 10 mm rectangular pieces with the long axis, i.e., the current direction, along the MgO [100] direction for each of the samples [see Fig. 3(b) below]. Four electrical contacts are attached to every piece along the long axis by ultrasonic wire bonding. We note that our AMR measurements were performed *ex situ* and because of the formation of a thin oxide layer on top of the Ni we can hence neglect the magnetocrystalline anisotropy resulting from steps as well as from under-coordinated surface sites [15].

III. RESULTS AND DISCUSSION

A. Magnetic anisotropy

The anisotropic surface roughness, which is generated by the oblique incidence of the ion beam, induces UMA which can be calculated using the "self-correlation function" based method [24,25]. According to this method, the UMA generated by dipolar stray fields can be inferred from the surface height profiles obtained from the STM topography images. The appropriate two-dimensional correlation function $g(x,y)$ [24], allows us to characterize the anisotropic surface roughness obtained from the STM images. Figures 1(e)–1(h) present plots of the self-correlation function $g(x,y)$ for our four samples. The map of $g(x,y)$ for the as-grown Ni film [Fig. 1(e)] is almost isotropic, and the small peak at the center indicates a quite flat surface due to the presence of the flat terraces in Fig. 1(a). On the other hand, the relatively high peak at the center of Fig. 1(f) reflects the increased roughness due to the mound structures appearing in Fig. 1(b), while the two crossing stripes in Fig. 1(f) reflect that the local topography is highly correlated in both directions resulting from the more or less rectangular shape of the mound structures. The pronounced parallel stripes in Figs. 1(g) and 1(h) are due to the presence of the ripple structures in Figs. 1(c) and 1(d), which results in a strongly anisotropic roughness. The higher peak at the center of Fig. 1(h) than at the center of Fig. 1(g) results from the larger local roughness in Fig. 1(d) than in Fig. 1(c).

The calculated anisotropy constants K_s, which give the strength of the shape anisotropy resulting from the anisotropic surface roughness, are summarized in Table I [24]. We note that the anisotropy due to anisotropic surface roughness of the as-grown Ni film is negligible, while K_s of sample 2 reflects the shape anisotropy due to the more or less rectangular mound structures appearing at the surface in Fig. 1(b). The easy axis resulting from the magnetic shape anisotropy in samples 3 and 4 is oriented along the grooves of the ripple structures.

B. Magnetization reversal

In Fig. 2 we present for each of the samples the hysteresis loops obtained from the AMR measurements at RT for

TABLE I. Summary of magnetic fitting parameters for samples 1, 2, 3, and 4. The parameters K_u and ε_{90° for sample 1 and 2 are obtained by fitting the angular dependence of the switching fields using the two-jump domain wall motion model. The parameters K_u and K_1 for samples 3 and 4 are obtained by fitting of the hysteresis loops along the hard axis using the coherent-rotation model. K_s is calculated by relying on the self-correlation method which uses the STM topography images (see text).

Sample	$K_u(10^4 \mathrm{erg/cm^3})$	$K_s(10^4 \mathrm{erg/cm^3})$	$K_1(10^4 \mathrm{erg/cm^3})$	$\varepsilon_{90^\circ}(10^4 \mathrm{erg/cm^3})$
sample 1	0.47 ± 0.12	0.07		1.92 ± 0.16
sample 2	0.47 ± 0.12	0.64		1.92 ± 0.16
sample 3	1.90 ± 0.20	2.69	6.20 ± 0.20	
sample 4	1.60 ± 0.20	1.92	5.70 ± 0.20	

magnetic field directions along the [100], [110], and [010] directions of the substrate (and also of the Ni films). The magnetization reversal occurs with a two-jump process along the [100] and [010] directions for samples 1 and 2 [26]. On the other hand, the hysteresis loops become continuous along the [100] and [010] directions for samples 3 and 4. The presented results demonstrate that the magnetization reversal mechanism is modified by the ripple structure formation on the surface. The resistance reaches a minimum for M $\parallel$ [110], contradicting the conventional $\cos^2\varphi$ dependence. This will be discussed in more detail below.

The dependence of the switching fields for the magnetization jumps during magnetization reversal on the applied field direction is summarized in Fig. 3(a) for samples 1 and 2. The angular dependence clearly reveals fourfold symmetry with the hard axis along the $\langle 100\rangle$ directions and the easy axis along the $\langle 110\rangle$ directions. Taking into account both the magnetocrystalline anisotropy and the UMA, the total free energy density is given by [8]

$$E = K_1 \cos^2\left(\theta + \frac{\pi}{4}\right)\cos^2\left(\theta - \frac{\pi}{4}\right) + K_u \sin^2(\theta - \phi_u) - \mu_0 M_S H \cos(\theta - \varphi), \quad (1)$$

where θ, ϕ_u, and φ denote the angles of the magnetization, the easy axis of the UMA, and the applied field with respect to the MgO [100] direction [see the schematic representation in Fig. 3(b)]. K_1 and K_u are the magnetocrystalline anisotropy constant and the UMA constant, respectively. We rely on the two-jump domain wall motion model to explain the magnetization reversal in samples 1 and 2 [8,26]. ϕ_u is fixed at $3\pi/4$ according to the larger magnitude of the lower switching field (H_{c1}) for $\varphi = 3\pi/4$ than for $\varphi = \pi/4$. The experimental azimuthal angular dependence of the switching fields can be nicely fitted [see solid lines in Fig. 3(a)], and the 90° domain wall pinning energy ε_{90° and K_u obtained from the

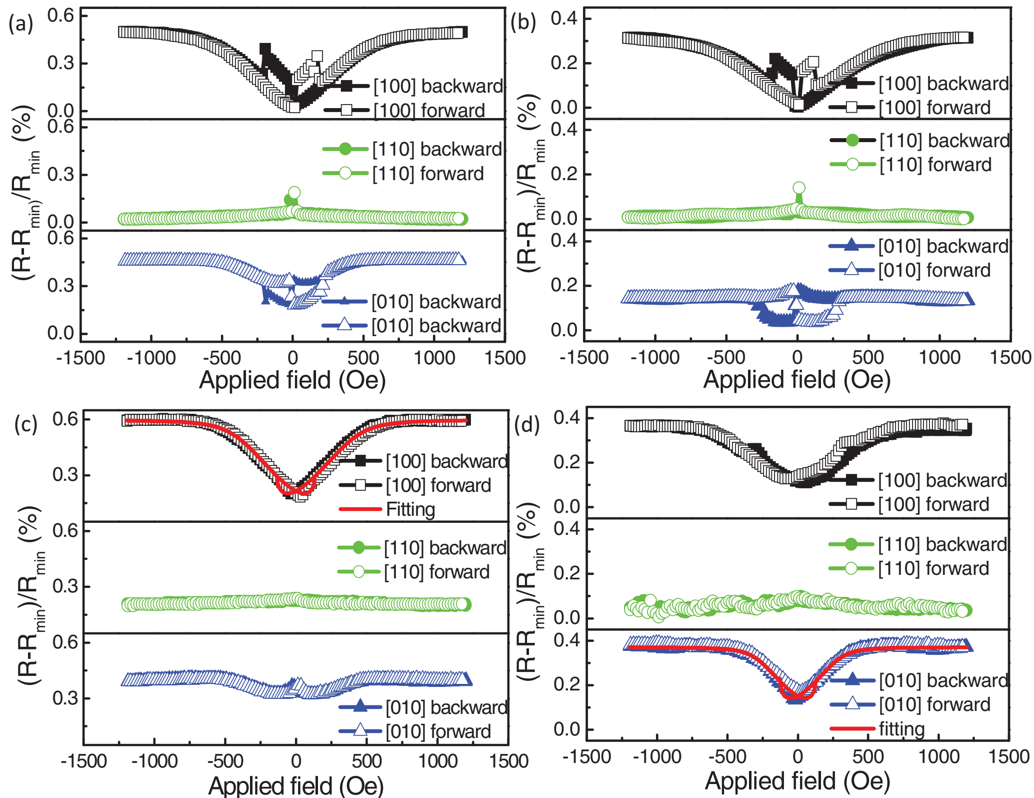

FIG. 2. (Color online) (a)–(d) Hysteresis loops obtained from the AMR measurements at RT along the [100], [110], and [010] directions for samples 1, 2, 3, and 4, respectively. The solid lines in (c) and (d) are simulated AMR curves based on the coherent-rotation model.

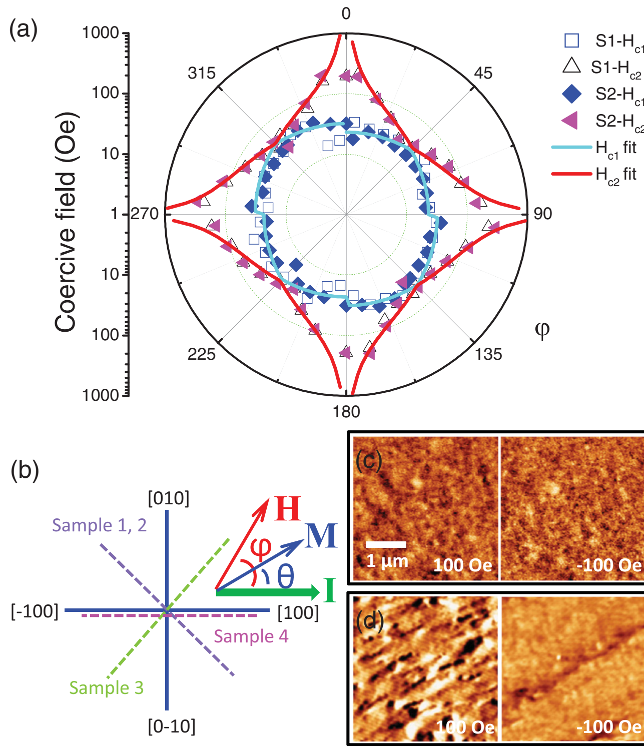

FIG. 3. (Color online) (a) Polar plots of switching fields as a function of the azimuthal angle for samples 1 and 2. The solid lines are fitted curves according to the model for two-jump domain wall motion. (b) Schematic representation of the orientations of the applied field, the current, and the crystallographic directions. The dotted lines denote the easy axes corresponding to the UMA (ϕ_u) for our four samples. (c) and (d) present the magnetic domain structures as measured by MFM for sample 1 and sample 3 with the applied fields along the [100] direction of the MgO substrate. The magnitude of the applied field is indicated in the lower right corner of each of the MFM images.

fitting are summarized in Table I. Based on the available experimental results for the azimuthal angular dependence of the AMR hysteresis loops, it is not possible to reliably determine the magnetocrystalline anisotropy constant K_1 for the samples 1 and 2. We note that the constant K_1 can eventually be determined accurately by other types of transport measurements based on the anomalous and planar Hall effects with the applied field perpendicular to the film plane [27].

The values of the switching fields for samples 1 and 2 are quite similar in Fig. 3(a) (within an experimental error of 20 Oe), leading to the same magnetic fitting parameters, although the calculated magnetic shape anisotropy constants K_s are quite different. The influence of magnetic shape anisotropy appears to be overwhelmed by magnetocrystalline anisotropy during magnetization reversal for both sample 1 and sample 2. The very small UMA in the as grown films may originate from the presence of surface steps and/or of under-coordinated surface sites [4,28]. The magnetic anisotropy constants of samples 3 and 4 can be obtained by fitting the hysteresis loops along the hard axis ([100] for sample 3 and [010] for sample 4) using the coherent-rotation model combined with Eq. (5) which is introduced below. The fitting curves are given by the solid lines in Figs. 2(c) and 2(d). ϕ_u is fixed at $\pi/4$ and at 0 for sample 3 and sample 4, respectively, i.e., along the grooves of the ripple structures. In the simulation for sample 4 we need to take into account an experimental error resulting from a misalignment between the ripple direction and the MgO [100] direction which is about 8°. Based on the comparable values of K_u and K_s in Table I for samples 3 and 4, we conclude that the UMA inferred from the magnetization reversal is dominated by the anisotropic surface roughness resulting from the grazing-incidence ion beam sputtering [7,12].

Figures 3(c) and 3(d) present the in-field magnetic domain structure as measured by magnetic force microscopy (MFM) for samples 1 and 3 with applied fields approximately along the [100] direction of the MgO substrates (deviation below 10°). Magnetization nucleates randomly with the formation of bubblelike domains and then further proceeds by domain wall motion during magnetization reversal for sample 1. For sample 3, however, magnetization reversal starts by nucleation of magnetic domains with domain walls oriented parallel to the grooves of the ripple structures and then further proceeds by domain wall motion. The magnetization reversal has already been largely completed at 100 Oe, except for some residual pinning of domain walls along the ripples. The existence of additional magnetic domain structures other than stripes along the ripples (MFM image at 100 Oe for sample 3) suggests that the magnetocrystalline anisotropy still plays a non-negligible role during magnetization reversal [29]. The magnetic domain structures of sample 2 and of sample 4 are similar to the domain structures of sample 1 and of sample 3, respectively.

C. Azimuthal angular dependence of the AMR

The azimuthal angular dependence of the AMR can be clearly observed when the resistance is measured for different applied field directions, but with a fixed magnitude exceeding the saturation field. In that case the direction of the magnetization (given by the angle θ) should be the same as that of the applied field (given by the angle φ). In Fig. 4 we present the relative resistance change $(R - R_{\min})/R_{\min}$ for the four samples as a function of the angle between current and applied field with a constant field magnitude of 1000 Oe at RT and 4000 Oe at LT. $R_{\min}$ is the minimum resistance. The higher field magnitude at LT is required to take into account the increase of the saturation field at LT. The shapes of the AMR curves clearly deviate from the simple $\cos^2\varphi$ dependence which results in twofold symmetry of the AMR curve and is observed in polycrystalline materials. Apart from the twofold symmetry our AMR curves clearly contain contributions of fourfold symmetry [$\cos^4\varphi$ dependence, see Eq. (5) below]. We note that the AMR amplitudes in Fig. 4 are reduced by a factor of 2 to 4 when compared to polycrystalline films [30]. Moreover, the angular dependence of the AMR changes for each of the four samples when going from RT to LT. Since the film thickness is quite similar for the four samples, we conclude that the different angular dependence of the AMR originates from the changes in the surface morphology induced by the ion beam sputtering.

In order to analyze our data for the azimuthal angular dependence, we rely on a phenomenological model based on

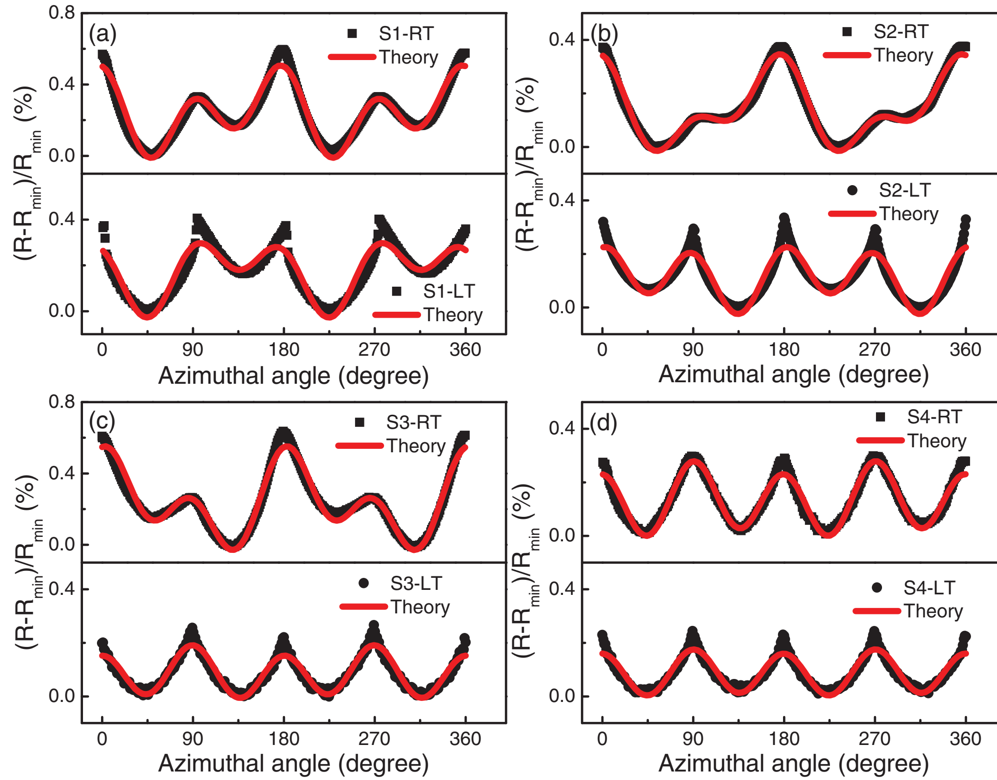

FIG. 4. (Color online) (a)–(d) Azimuthal angular dependence of the AMR at RT and at LT for samples 1, 2, 3, and 4. The constant magnitude of the applied field is 1000 Oe for the measurements at RT and 4000 Oe for the measurements at LT.

crystal symmetry as proposed by Döring [17]. This model has been successfully used before to describe the angular dependence of the AMR in Ni and Fe single crystals [17,18]. According to Ohm's law, an electric field component E_i is produced when a current J_j flows along the spatial direction j and the relation between current and field can be expressed as: $E_i = \rho_{ij}(\alpha)J_j$. The resistivity tensor ρ_{ij} is a function of the direction cosines α_i of magnetization and can be expanded in a Maclaurin series

$$\rho_{ij} = a_{ij} + a_{ijk}\alpha_k + a_{ijkl}\alpha_k\alpha_l + \cdots , \tag{2}$$

where a_{ij}, a_{ijk}, and a_{ijkl} are the elements of different orders of the resistivity tensor. The resistivity tensor can be simplified due to the crystal symmetry and Onsager's theorem, which results in [16]

$$\begin{aligned}\frac{\rho-\rho_0}{\rho_0} = {} & k_1\left(\alpha_1^2\beta_1^2+\alpha_2^2\beta_2^2+\alpha_3^2\beta_3^2-\frac{1}{3}\right)\\ & +2k_2(\alpha_1\alpha_2\beta_1\beta_2+\alpha_2\alpha_3\beta_2\beta_3+\alpha_3\alpha_1\beta_3\beta_1)\\ & +k_3 s+k_4\left(\alpha_1^4\beta_1^2+\alpha_2^4\beta_2^2+\alpha_3^4\beta_3^2+\frac{2}{3}s-\frac{1}{3}\right)\\ & +2k_5\big(\alpha_1\alpha_2\alpha_3^2\beta_1\beta_2+\alpha_2\alpha_3\alpha_1^2\beta_2\beta_3\\ & +\alpha_3\alpha_1\alpha_2^2\beta_3\beta_1\big),\end{aligned} \tag{3}$$

where $\rho_0 = a_{11} + a_{1122} + a_{111122}$, $k_1 = k_1' - k_3'$, $k_2 = 2k_4'$, $k_3 = k_3'$, $k_4 = k_2' + k_3'$ and $k_5 = 2k_5'$. The constants k_i' are given by

$$\begin{aligned} k_1' &= a_{111} - a_{1122} - 2a_{111122} + a_{112211},\\ k_2' &= a_{111111} + a_{1122} - a_{112211},\\ k_3' &= a_{112233} - a_{111122},\\ k_4' &= a_{2323} + a_{111212},\\ k_5' &= a_{112323} - a_{111212},\end{aligned} \tag{4}$$

β_i is the direction cosine of the current with respect to the cubic axes, and s is defined as $s = \alpha_1^2\alpha_2^2 + \alpha_2^2\alpha_3^2 + \alpha_3^2\alpha_1^2$. For our specific geometry the magnetization lies in the (001) film plane with $\alpha_1 = \cos\theta, \alpha_2 = \sin\theta, \alpha_3 = 0$, while the current is along the [100] direction with $\beta_1 = 1$, $\beta_2 = 0$, $\beta_3 = 0$. Equation (2) can then be simplified to

$$\frac{\rho-\rho_0}{\rho_0} = C_0 + C_1\cos^2(\theta+\delta) + C_2\cos^4\theta\ , \tag{5}$$

where $C_0 = \frac{1}{3}(k_1 - k_4)$, $C_1 = k_1 + k_3 + \frac{2}{3}k_4$, $C_2 = k_4/3 - k_3$, and the angle δ is added to take into account a small misalignment between the actual current direction and the nominal [100] direction of the substrate. Using Eq. (5) the azimuthal angular dependence of the AMR can be very well fitted for the four samples, both at RT and LT (see solid lines in Fig. 4). From the fitting we obtain the values of k_1, k_3, and k_4 for the four samples at RT and at LT, as listed in Table II. The coefficients k_i depend on the crystal symmetry and also depend on temperature because the dominant electron scattering mechanisms depend on temperature [15]. When comparing the obtained k_i values to the corresponding values for bulk Ni [17],

TABLE II. Summary of the coefficients of the phenomenological model derived by fitting the azimuthal angular dependent AMR curves in Fig. 4 using Eq. (5).

Sample	k_1	k_3	k_4	δ
sample 1 (RT)	0.0056	−0.0144	−0.0038	−4.62°
sample 2 (RT)	0.0014	−0.0060	−0.0011	−5.51°
sample 3 (RT)	0.0055	−0.0141	−0.0023	4.61°
sample 4 (RT)	0.0045	−0.0109	−0.0037	−5.15°
sample 1 (LT)	0.0034	−0.0094	−0.0038	−0.79°
sample 2 (LT)	0.0027	−0.0089	−0.0031	2.84°
sample 3 (LT)	0.0031	−0.0099	−0.0035	0.53°
sample 4 (LT)	0.0026	−0.0092	−0.0029	−0.42°
bulk (RT)	0.0065	−0.0036	−0.0051	

we need to take into account the influence of additional surface scattering and defects in our films [15,17]. The different values of δ at RT and LT for the same sample are related to the fact that due to practical reasons the samples need to be remounted for the measurements at LT after the measurements at RT. We note that a similar temperature dependence of the parameters k_i is consistently obtained for films prepared at different times, confirming the reproducibility of the results presented in Fig. 4. While the exact value of δ may change for samples prepared and/or mounted at different times, the relative weight of the twofold and fourfold symmetries of the angular dependence of the AMR does not reveal any correlation with the values obtained for the fitting parameter δ.

The obtained values of k_1, k_3, and k_4 at RT indicate that the ripple structure along the [110] direction on the surface mainly results in a decrease of the value of k_4 for sample 3. On the other hand, the ripple structure along the [100] direction mainly gives rise to a decrease of the values for k_1 and k_3 for sample 4. The different influence of the two ripple structures can be related to a different impact on the crystal symmetry, resulting in a different relative weight of the $\cos^2 \varphi$ and $\cos^4 \varphi$ terms in Eq. (5) [16]. Finally, the mound structures on the surface of sample 2 result in a significant decrease of k_1 as well as of k_3 and k_4. The latter decrease of the k_i by the surface morphology can be attributed to the presence of additional diffuse surface scattering, which is consistent with the enhanced surface roughness of sample 2 and accounts for a reduced impact of the crystal symmetry on the AMR effect.

The AMR results presented in Fig. 4 also reveal that the obtained k_i values become comparable for all four samples at LT, which reflects a pronounced influence of temperature on the k_i. On the other hand, we find that the k_i values are smaller at LT than at RT, except for sample 2 for which the k_i values become larger. Except for sample 2, the resulting amplitude of the AMR clearly becomes smaller at LT than at RT, a behavior which is opposite to what has been found for other systems [15,19,20]. The underlying physical mechanisms which govern the AMR at different temperatures and the exact relationship between the AMR and the coefficients k_i still needs to be investigated in detail using first principles calculations [31]. Anyway, our AMR results clearly confirm the direct impact of the ion sputtering process on the azimuthal angular dependence of the AMR. In particular, a ripple structure along the [100] hard axis results in a pronounced influence of the magnetocrystalline anisotropy already at RT, giving rise to a dominating fourfold symmetry of the angular dependence [see Fig. 4(d)]. On the other hand, a ripple structure along the [110] easy axis results in an decreased influence of magnetocrystalline anisotropy at RT, giving rise to an increased twofold symmetry and a larger AMR amplitude. We succeeded here in modifying in a controllable way the relative weight of the twofold and fourfold symmetries of the AMR by grazing-incidence ion beam sputtering along different crystallographic directions of epitaxially grown thin films.

IV. CONCLUSIONS

The magnetic anisotropy, magnetization reversal and anisotropic magnetoresistance have been tailored in Ni films grown on MgO (001) substrates by modifying the surface morphology using ion beam sputtering. The ripple structures, which can be induced on the surface by grazing-incidence ion beam sputtering, give rise to uniaxial magnetic anisotropy mainly originating from dipolar stray fields. The ripples act as domain wall nucleation and pinning sites during magnetization reversal, while two-jump domain wall motion dominates in the as-grown Ni films. The azimuthal angular dependence of the AMR reflects a superposition of fourfold and twofold symmetry and can be described by a phenomenological model based on the crystal symmetry. The relative weight of the fourfold and twofold symmetry can be modified by grazing incident ion beam sputtering along specific crystallographic directions. The here achieved “tailoring” of the magnetic anisotropy, magnetization reversal, and AMR by ion beam sputtering may be used for the design of electron transport based magnetic sensors and other spintronic devices.

ACKNOWLEDGMENTS

This work has been supported by the Research Foundation Flanders (FWO) as well as by the Flemish Concerted Research Action program (BOF KU Leuven, project GOA/14/007) and the Flemish Hercules Foundation (project AKUL 09/042).

[1] W. Weber, C. H. Back, A. Bischof, C. Würsch, and R. Allenspach, Phys. Rev. Lett. **76**, 1940 (1996).
[2] A. Berger, U. Linke, and H. P. Oepen, Phys. Rev. Lett. **68**, 839 (1992).
[3] J. Chen and J. L. Erskine, Phys. Rev. Lett. **68**, 1212 (1992).
[4] J. H. Gao, Y. Girard, V. Repain, A. Tejeda, R. Belkhou, N. Rougemaille, C. Chacon, G. Rodary, and S. Rousset, Phys. Rev. B **77**, 134429 (2008).
[5] R. M. Bradley and J. M. E. Harper, J. Vac. Sci. Technol. A **6**, 2390 (1988).

[6] R. Moroni, D. Sekiba, F. Buatier de Mongeot, G. Gonella, C. Boragno, L. Mattera, and U. Valbusa, Phys. Rev. Lett. **91**, 167207 (2003).
[7] K. Chen, R. Fromter, S. Rossler, N. Mikuszeit, and H. P. Oepen, Phys. Rev. B **86**, 064432 (2012).
[8] Q. F. Zhan, S. Vandezande, C. Van Haesendonck, and K. Temst, Appl. Phys. Lett. **91**, 122510 (2007).
[9] K. Zhang, M. Brotzmann, and H. Hofsäss, New J. Phys. **13**, 013033 (2011).
[10] F. Bisio, R. Moroni, F. Buatier de Mongeot, M. Canepa, and L. Mattera, Phys. Rev. Lett. **96**, 057204 (2006).
[11] M. O. Liedke, M. Korner, K. Lenz, F. Grossmann, S. Facsko, and J. Fassbender, Appl. Phys. Lett. **100**, 242405 (2012).
[12] M. O. Liedke, M. Korner, K. Lenz, M. Fritzsche, M. Ranjan, A. Keller, E. Cizmar, S. A. Zvyagin, S. Facsko, K. Potzger, J. Linder, and J. Fassbender, Phys. Rev. B **87**, 024424 (2013).
[13] J. Smit, Physica **16**, 612 (1951).
[14] R. I. Potter, Phys. Rev. B **10**, 4626 (1974).
[15] R. P. van Gorkom, J. Caro, T. M. Klapwijk, and S. Radelaar, Phys. Rev. B **63**, 134432 (2001).
[16] T. R. McGuire and R. I. Potter, IEEE Trans. Magn. **MAG-11**, 1018 (1975).
[17] W. Döring, Ann. Phys. (Leipzig) **32**, 259 (1938).
[18] E. Fawcett and W. A. Reed, Phys. Rev. Lett. **9**, 336 (1962).
[19] Y. Bason, J. Hoffman, C. H. Ahn, and L. Klein, Phys. Rev. B **79**, 092406 (2009).
[20] D. Wu, P. Wei, E. J. Halperin, D. D. Awschalom, and J. Shi, Phys. Rev. B **77**, 125320 (2008).
[21] P. Li, E. Y. Jiang, and H. L. Bai, Appl. Phys. Lett. **96**, 092502 (2010).
[22] T. Skeren, K. Temst, W. Vandervorst, and A. Vantomme, New J. Phys. **15**, 093047 (2013).
[23] S. Brems, K. Temst, and C. Van Haesendonck, Phys. Rev. Lett. **99**, 067201 (2007).
[24] J. L. Bubendorff, S. Zabrocki, G. Garreau, R. Jaafar, D. Berling, A. Mehdaoui, C. Pirri, and G. Gewinner, Europhys. Lett. **75**, 119 (2006).
[25] H. L. Liu, W. He, Q. Wu, H. T. Yang, X. Q. Zhang, and Z. H. Cheng, AIP Adv. **3**, 062101 (2013).
[26] R. Cowburn, S. Gray, J. Ferré, J. Bland, and J. Miltat, J. Appl. Phys. **78**, 7210 (1995).
[27] H. X. Tang and M. L. Roukes, J. Phys.: Condens. Matter. **19**, 165206 (2007).
[28] D. S. Chuang, C. A. Ballentine, and R. C. O'Handley, Phys. Rev. B **49**, 15084 (1994).
[29] T. Taniuchi, H. Kumigashira, M. Oshima, T. Wakita, T. Yokoya, M. Kubota, K. Ono, H. Akinaga, M. Lippmaa, M. Kawasaki, and H. Koinuma, Appl. Phys. Lett. **89**, 112505 (2006).
[30] I. Rhee and C. Kim, IEEE Trans. Magn. **37**, 1032 (2001).
[31] W. Gil, D. Görlitz, M. Horisberger, and J. Kötzler, Phys. Rev. B **72**, 134401 (2005).